Isospin ferromagnetism and momentum polarization in bilayer graphene

Zhiyu Dong, Margarita Davydova, Olumakinde Ogunnaike, Leonid Levitov
Massachusetts Institute of Technology, Cambridge, Massachusetts 02139, USA
(Dated: November 2, 2021)

Electron bands in Bernal-stacked (nontwisted) graphene bilayers in a transverse electric field feature field-tunable bandgaps and band dispersion that flattens out as the field increases. The effects of electron interactions are sharply enhanced in this regime, leading to a cascade of correlated phases exhibiting isospin (spin-valley) and momentum polarization orders. The momentum polarization, driven by exchange interactions, originates from a "flocking" effect, wherein all carriers condense into one, two or three pockets produced by the trigonal warping of the electron bands. The isospin-polarized phases mimic many aspects of the phases found in moiré graphene. The momentum-polarized phases, to the contrary, have symmetry lower than that of the isospin-polarized phases in moiré bands. We identify effects that can serve as probes of these orders, such as electronic nematicity, a $B = 0$ anomalous Hall response and orbital magnetization.

Narrow bands in moiré graphene [1–4] host a variety of strongly correlated phases with exotic properties that can be accessed by tuning external fields and carrier density [5–26]. These findings inspired investigations into the existence of other narrow-band systems with interesting properties. Recently, two nontwisted graphene multilayers—Bernal-stacked bilayers and ABC trilayers—have been identified [27, 28] as systems showing cascades of ordered phases resembling those seen in moiré graphene [37–41]. These systems feature electron bands with field-tunable bandgaps and dispersion that flattens out quickly as the field increases. Carriers in these bands become nearly dispersionless at large fields, forming strongly interacting systems with interesting properties [29–36]. These developments prompted questions about new symmetry breaking types and new orders achievable in these systems.

Here, starting from a simple framework for the interaction effects, we predict new order types with properties considerably richer than those of isospin-ordered phases. We focus on the Bernal-stacked bilayer graphene (BG) in a transverse electric field, arguably the simplest system with field-tunable bands. Field-biased BG features bands with field-induced bandgaps and dispersion that flattens out quickly as the field increases. Expectedly, strong interactions of carriers in flattened bands drive isospin (spin-valley) polarization instability and a cascade of phase transitions between states with different polarizations, resembling those known in moiré graphene [37–41]. A phase diagram for this cascade is shown in Fig 1 a).

Strikingly, a sharp change in behavior occurs at lower densities and stronger fields, where interactions lead to an isospin-polarized Fermi sea break-up and spontaneous momentum polarization, as illustrated in Fig 1 b). The momentum polarization originates from exchange-induced "flocking" effect, wherein all carriers condense into one, two or three pockets at the band minima produced by the trigonal warping interactions. Momentum-polarized phases emerge out of isospin-polarized phases that act as their mother states. We describe symmetry breaking transitions leading to these orders, and their unique signatures such as electronic nematicity and incommensurate Kekulé-type density waves. Furthermore, a redistribution of Berry curvature throughout the con-

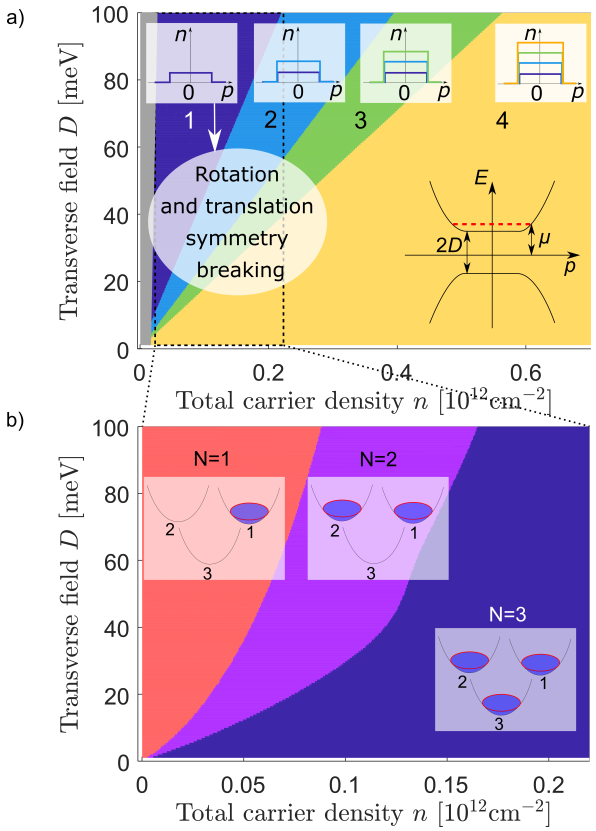

FIG. 1. a) Phase diagram for different isospin (valley and spin) orders in a lightly-doped field-biased BG band. Carriers form Fermi seas with the degree of isospin polarization increasing with field bias. States with different numbers of isospin species, pictured in the insets, are found in the four regions of the phase diagram obtained using realistic parameters. Polarization degree varies from one layer (fully polarized) to four layers (unpolarized) [see text beneath Eq. (7)]. b) Level-two symmetry breaking occurring in a dashed box marked in a). Different orders arise due to the Fermi sea spontaneously breaking into $N = 1$, 2 or 3 pockets and shifting to different band minima [see text after Eq. (15)].

duction band resulting from its trigonal warping endows the momentum-polarized states with an enhanced anomalous Hall response (see Fig 2). An abrupt onset of a $B = 0$ Hall effect, along with anisotropy of transport due to electronic nematicity, will provide clear signatures of momentum-polarized ordered states.

Electron bands of field-biased BG can be modeled with a parabolic Dirac problem accounting for low-energy states near K and K' points[42–44]:

$$H_0 = \sum_p \Psi^\dagger_{\boldsymbol{p}} h_0(\boldsymbol{p}) \Psi_{\boldsymbol{p}}, \tag{1}$$
$$h_0(\boldsymbol{p}) = -\frac{p_1^2 - p_2^2}{2m} 1_\tau \sigma_1 - \frac{2p_1 p_2}{2m} \tau_3 \sigma_2 + D 1_\tau \sigma_3,$$

where $\Psi_{\boldsymbol{p}} = (\psi_{AK\boldsymbol{p}}, \psi_{BK\boldsymbol{p}}, \psi_{AK'\boldsymbol{p}}, \psi_{BK'\boldsymbol{p}})^{\mathrm{T}}$, $\tau_{1,2,3}$ and $\sigma_{1,2,3}$ are the Pauli matrices acting on the valley and sublattice (layer) degrees of freedom, respectively. For conciseness, we have suppressed the spin indices for now, as the spin-orbit coupling is negligible. The quantity D is the interlayer bias generated by the transverse electric field. Subleading terms[44], such as trigonal warping, are ignored for now as we focus on understanding the emergence of the ordered phases in $SU(4)$-symmetric model. These terms govern subtle effects such as isospin anisotropy and momentum polarization, see below.

Here, we will be interested in the regime where the field-induced bandgap $2D$ is large compared to the carrier kinetic energy (see inset in Fig. 1 a)). In this regime the upper and lower bands, flattened and separated by the energy $2D \gg \mu$, effectively decouple. We therefore project the problem onto the conduction band [47]

$$E(\boldsymbol{p}) = \sqrt{D^2 + \left(\frac{p^2}{2m}\right)^2} \tag{2}$$

and take the electron-electron interaction to be an isospin-independent density-density coupling of carriers in this band,

$$\tilde{H}_{int} = \frac{1}{2} \sum_{\boldsymbol{p}\boldsymbol{p}'\boldsymbol{q}} V_{\boldsymbol{q}} \tilde{\psi}^\dagger_{i,\boldsymbol{p}} \tilde{\psi}^\dagger_{j,\boldsymbol{p}'} \tilde{\psi}_{j,\boldsymbol{p}'-\boldsymbol{q}} \tilde{\psi}_{i,\boldsymbol{p}+\boldsymbol{q}}. \tag{3}$$

Here $\tilde{\psi}_{i,\boldsymbol{p}}$ are field operators of conduction electrons, with i and j the isospin components $K\uparrow$, $K\downarrow$, $K'\uparrow$, $K'\downarrow$. This Hamiltonian has a clear isospin $SU(4)$ symmetry.

To gain insight into the parameter regime for isospin polarization occurs we use a simple constant interaction model, refining it in the subsequent analysis of momentum polarized order. The isospin order is a result of a Stoner instability arising from the exchange energy, which can be written as

$$E_{ex} = -\frac{1}{2} \sum_{i\boldsymbol{p}\boldsymbol{p}'} V_{\boldsymbol{p}-\boldsymbol{p}'} n_{i\boldsymbol{p}} n_{i\boldsymbol{p}'}, \tag{4}$$

where i indexes isospin as in Eq.(3). Below, for simplicity, we model the interaction as a local interaction, $V_{\boldsymbol{p}-\boldsymbol{p}'} = V$. The onset of $SU(4)$ isospin polarization is determined by the Stoner criterion:

$$V\nu = 1, \tag{5}$$

with the density of states ν in the conduction band,

$$\nu = \frac{m}{2\pi} \frac{\mu}{\sqrt{\mu^2 - D^2}} \approx \frac{m^2}{(2\pi)^2} \frac{D}{n}. \tag{6}$$

Here we have used the expression for the electron density in the single-electron picture, $n = \frac{m}{2\pi}\sqrt{\mu^2 - D^2}$, taking the chemical potential to lie near the bottom of the band, $\mu \sim D$. With this, we estimate the carrier density at the onset of the Stoner instability, finding a fan of phase boundaries n vs. D for $M = 1$, 2 or 3 isospin species:

$$n_D = M \frac{V m^2 D}{(2\pi)^2}. \tag{7}$$

For BG parameters $m = 0.028 m_e$[42–44], $V = 10^3\,\mathrm{meV\,nm^2}$ [47], this simple model predicts an isospin ordering transition at carrier densities $n_D \sim 10^{12}\mathrm{cm}^{-2}$ for the values of the interlayer bias $D = 100$ meV, in good agreement with Ref.[27].

The resulting phase diagram, obtained by comparing energies of partially polarized states with $M = 1$, 2, 3 and 4 isospin species, is shown in Fig. 1 a). The inset in the lower right corner shows electron dispersion near charge neutrality, with the Fermi level marked by a red dashed line. The yellow area represents the disordered phase where all four isospin species are equally filled. Purple, light blue and green mark stability regions for isospin-ordered states. The insets at the top illustrate the layer-cake structure of electron distribution in each of the phases, with the Fermi seas for different isospin species shown in different colors. The gray region near charge neutrality marks the band insulator phase with an unoccupied conduction band. The dashed rectangle marks the region of low carrier density on which the second half of this paper will focus. As we will see, trigonal warping of the conduction band flattened by the external field D gives rise to Fermi sea breakups and level-two symmetry breaking through spontaneous momentum polarization. This behavior is summarized in the phase diagram in Fig. 1 b).

Because of the $SU(4)$ symmetry of our model, the phase diagram in Fig. 1 a) is insensitive to the order parameter orientation in the isospin space. However, in reality, small valley anisotropy in the Hamiltonian, e.g. trigonal warping or intervalley scattering, can lift the $SU(4)$ degeneracy and favor a certain orientation in isospin space. These competing effects will be discussed elsewhere. Yet, the symmetry aspects of different orders can be understood very generally without detailed knowledge of the order that is ultimately favored. Table I summarizes the results of our symmetry analysis[47] for phase 1 (fully polarized isospin). In this case there are two possible phases, O_1^z and O_1^{xy}, describing orders with

irreps	matrices	O_1	broken symmetries	Ohmic conductivity	spatial modulation	Hall conductivity
$A_{2,\Gamma}$, 1D	τ_3	$O_1^z = P_\tau^{\pm z} P_s^{\boldsymbol{m}}$	mirror, time reversal	isotropic	none	nonvanishing
$E_{\pm K}$, 2D	(τ_1, τ_2)	$O_1^{xy} = P_\tau^{\boldsymbol{\gamma}} P_s^{\boldsymbol{m}}$	rotation, mirror, translation	anisotropic	Kekulé order	vanishing

TABLE I. Symmetry classification of different isospin orders. Listed are results for two real irreducible representations (irreps) of the field-biased BG space group under which the valley-space Pauli matrices $\tau_{1,2,3}$ can transform; other irreps are not realized by isospin-polarized orders. Column 1 lists the irreps and their dimensions. In column 3, the projection operators in valley and spin space constituting the order parameter are: $P_\tau^{\pm z} = \frac{1}{2}(1 \pm \tau_3)$, $P_\tau^{\boldsymbol{\gamma}} = \frac{1}{2}(1 + \gamma_1\tau_1 + \gamma_2\tau_2)$, $P_s^{\boldsymbol{m}} = \frac{1}{2}(1 + \boldsymbol{s}\cdot\boldsymbol{m})$, where $\boldsymbol{\gamma} = (\gamma_1, \gamma_2)^{\mathrm{T}}$ with real $\gamma_{1,2}$, $\boldsymbol{m} = (m_1, m_2, m_3)^{\mathrm{T}}$ is an arbitrary three-dimensional real vector. Columns 4-7 list broken symmetries and signature observables (see text).

valley imbalance and intervalley coherence, respectively. These two order types break different symmetries and have different signature observables as a result.

Next, we turn to discussing momentum-polarized ordered states that are unique to field-biased BG. These orders arise through an instability in which an isospin-polarized Fermi sea breaks up into several distinct pockets that shift towards minima of the conduction band.

It is instructive to start with a qualitative discussion of how this instability comes into play. There is an anisotropy in a realistic BG bandstructure at small momenta due to the trigonal warping term, which is not included in the minimal description of band structure Eq. (1). This anisotropy leads to a three-pocket shape of Fermi surface in the regime of extremely low carrier density. As a result, for each isospin, instead of uniformly filling all three pockets, there are three candidate electron configurations for the ground state, in which either one, two or all three pockets are filled. Which one wins is determined by the competition between the kinetic and the exchange energy. The kinetic energy favors the configuration where all pockets are uniformly filled, whereas the exchange energy is optimized when all electrons are placed in the same pocket, since the interpocket exchange interaction is weaker than the intrapocket one.

To estimate of the energy scales that govern this competition, we consider the total single-particle kinetic energy for all carriers condensed in one pocket:

$$E_K \sim n^2/2\nu_*, \tag{8}$$

where $\nu_* \sim 5\times10^{-5}$ meV^{-1} nm^{-2} is the density of states at the bottom of a single pocket [47]. To study the pocket polarization, we take into account the momentum dependence of the interaction. Then the exchange part of the energy is:

$$E_{ex} \sim -\frac{2\pi e^2}{\kappa|\boldsymbol{p}|}n^2 \sim -\frac{\sqrt{\pi}}{\kappa}e^2 n^{3/2} \tag{9}$$

where the dielectric constant κ accounts for screening. We estimate the characteristic momentum scale $|p|$ as $|p| \sim \sqrt{4\pi n}$. As a result, the exchange energy dominates at sufficiently small density $n \lesssim n_* = \frac{4\pi}{\kappa^2}e^4\nu_*^2 \sim 10^{11}$ cm^{-2}, where we have used a realistic value $D \sim 100$ meV and $\kappa \sim 5$ similar to dielectric constant in monolayer graphene. The realistic κ values will depend on the experimental setup.

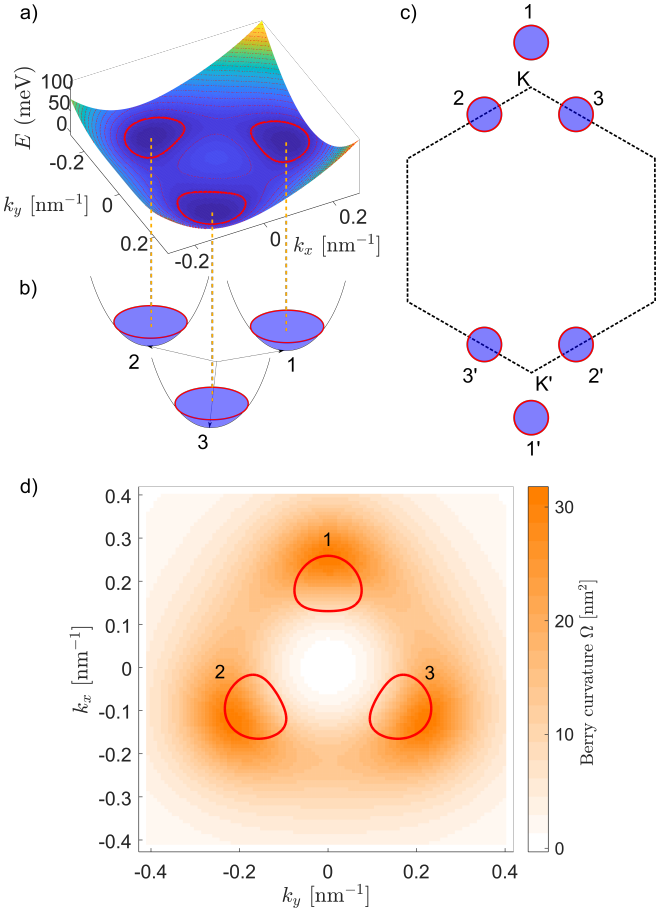

FIG. 2. a) Conduction band dispersion flattened by transverse field. Trigonal warping interaction creates three mini-valleys, at low carrier density giving rise to three electron pockets (red contours). b) A toy model for the three-pocket band structure. c) Schematic for pockets positioned near K and K' points. d) The distribution of the Berry curvature in the conduction band near K point. Parameters used: bias potential $D = 100$ meV, chemical potential $\mu = 90$ meV [47]. The value $\mu < D$ reflects the effect of the trigonal warping.

Next, we consider a simple model that accounts for pocket ordering and work out a phase diagram for realistic system parameters. We use a simple low-energy model consisting of three parabolic bands representing the three electron pockets in the conduction band:

$$H_i(\boldsymbol{p}) = (\boldsymbol{p} - \boldsymbol{k}_i)^2/2m_*, \tag{10}$$

where $i = 1, 2, 3$ labels the pockets, with the pocket centers $\boldsymbol{k}_i$ positioned at the three minima of the conduction band, $k_1 = k_*(0, 1)$, $k_{2,3} = k_*(\mp\sqrt{3}/2, -1/2)$. The k_* values and the effective masses m_* of the pockets are extracted from a realistic band structure [47].

For clarity, we focus on the effects arising in phase 1, where the additional effects of densities in different isospin states is absent. Here, there are three possible candidate ground states in which electrons fill up one, two or all three pockets. To determine which one of them is the true ground state, we compare their energies E_N ($N = 1, 2, 3$ is the number of occupied pockets) at the same total carrier density n. Their energies $E_N = E_K^{(N)} + E_{ex}^{(N)}$ consist of kinetic and exchange energy contributions. Using the fact that the density of states in each pocket is a constant $\nu_* = m_*/2\pi$, we can write the total kinetic energy as

$$E_K^{(N)} = \frac{N}{2\nu_*}\frac{n^2}{N^2} = \frac{\pi n^2}{N m_*} \tag{11}$$

In order to explore the pocket polarization, we restore the momentum dependence of the interaction in the exchange part of the free energy:

$$E_{ex}^{(N)} = -\frac{1}{2}\sum_{i,j=1}^{N}\sum_{\boldsymbol{p},\boldsymbol{p}'} V_{p-p'} n_{i\boldsymbol{p}} n_{j\boldsymbol{p}'}, \quad V_{\boldsymbol{p}-\boldsymbol{p}'} = \frac{2\pi e^2}{\kappa|\boldsymbol{p}-\boldsymbol{p}'|}, \tag{12}$$

where $n_{i\boldsymbol{p}}$ is the occupation number at momentum $\boldsymbol{p}$ measured relative to the pocket i center. For simplicity, as in Eq 9, we use momentum-independent dielectric constant κ. When the carrier density is small, the inter-pocket exchange interactions yield a nearly momentum-independent renormalization of the energy of each electron, which justifies approximating the Fermi surfaces in the pockets by discs centered at $\boldsymbol{k}_{*i}$. From this, we have

$$E_{ex}^{(N)} = -\frac{1}{2}\sum_{i,j=1}^{N}\sum_{\boldsymbol{p},\boldsymbol{p}'} V_{\boldsymbol{p}-\boldsymbol{p}'+\boldsymbol{k}_{ij}} n_{\boldsymbol{p}} n_{\boldsymbol{p}'}, \tag{13}$$

where $\boldsymbol{k}_{ij} = \boldsymbol{k}_i - \boldsymbol{k}_j$ are momentum differences between pocket centers, $n_{\boldsymbol{p}}$ is the occupation number of the state with momentum $\boldsymbol{p}$ measured relative to pocket center $n_{\boldsymbol{p}} = 1 - \theta(|p| - p_0)$. Here p_0 is the radius of the circular Fermi surface in each pocket

$$p_0 = \sqrt{4\pi n/N}. \tag{14}$$

With these expressions, the exchange energy can be evaluated analytically by performing the Fourier transform [47], giving

$$E_{ex}^{(N)} = -\frac{e^2 p_0^4}{16\pi}\sum_{ij}\int_0^\infty dr\,[J_2(rp_0) + J_0(rp_0)]^2\, J_0(r|k_{ij}|). \tag{15}$$

Our circular-pocket approximation is expected to be accurate when the distance k_* from pocket centers to K point is much greater than the pocket radius p_0. This yields an upper bound for carrier density: $n \lesssim 0.3\times 10^{12}$ cm^2, where we used the value of k_* estimated in [47]. As Fig. 1 a) indicates, the maximal density in phase 1 always satisfies the above validity condition. We can therefore use the results in Eqs. (11),(15) to determine the phase diagram by comparing the energies of one-pocket, two-pocket and three-pocket configurations.

The resulting pocket polarization phase diagram in the small density regime is shown in Fig. 1 b). At lowest carrier density, exchange energy dominates and all electrons prefer to condense in a single pocket. Upon carrier density increasing, the system undergoes phase transitions, first to a two-pocket configuration, and then to a three-pocket (unpolarized) phase. For illustration, in Fig. 1 b), we set the dielectric constant to be $\kappa = 2$, so that the phase diagram showcases all possible phases. The details of the phase diagram observed in experiment may vary from system to system, since the competition of pocket orders is sensitive to screening effects that depend on the experiment setup. If screening is made stronger [e.g. by a proximal gate], the pocket unpolarized state will be suppressed compared to that shown in Fig. 1 b). Alternatively, if the screening is made weaker, the pocket-polarized phase will expand, taking over a larger part of the phase diagram. We note that the energy difference between the pocket polarized and unpolarized states is of the order of 0.1meV to 1meV per carrier, yielding a readily accessible ordering temperature scale of a few kelvin.

Finally, we discuss manifestations of momentum-polarized states. Individual pocket can of course be identified through the quantum oscillations e.g. of magnetoresistance. The oscillation frequency as a function of inverse transverse magnetic field measures the area of the Fermi surface. Taken relative to the net carrier density, the oscillation frequency will be reduced by a factor of $1/N$ once N pockets form.

Crucially, the pocket-polarized states further break the crystallographic symmetries, leading to distinct effects that can be probed by the symmetry-sensitive measurements discussed above. Indeed, two possible orders of the parent phase, i.e. phase 1, correspond to two kinds of broken symmetries— either breaking only mirror symmetry, or breaking rotation, mirror and translation symmetries (see Table I). If phase 1 only breaks mirror symmetry, then populating one or two out of three pockets will further break the three-fold rotation symmetry without breaking the translation symmetry, leading to electron nematicity. This symmetry breaking can be observed by measuring the anisotropy in the conductivity. If, however, the parent isospin order is intervalley coherent, then the only remaining symmetry to be broken in the pocket-polarization transition is the translation symmetry. Namely, the pocket polarization on top of valley coherent states transforms the Kekulé charge density wave into an incommensurate density wave which carries momentum $P_{i,i'} = 2K + k_{*i} + k_{*i'}$, $i = 1, 2, 3$, $k_{*i'} = -k_{*i}$, see Fig. 2 c). In this case, the pocket order can be de-

tected by imaging long-period spatial modulations.

Pocket polarization can also be detected by measuring the Hall conductivity. When the pocket polarization happens on top of the valley imbalance order O_1^z which allows a nonvanishing Hall conductivity, the Hall conductivity changes abruptly since the Berry curvature is non-uniform near K point [see Fig. 2 d)]. If the pocket polarization occurs on top of O_1^{xy} isospin order, which originally respects the time reversal symmetry, enforcing a vanishing Hall conductivity, then the onset of the pocket polarization can break the time-reversal symmetry so long as electrons populate different pockets in valleys K and K' [e.g. pocket 1 and $2'$ in Fig. 2 c)]. As a result, the Hall conductivity will jump from zero to some finite value at the pocket ordering transition. Therefore, regardless of the form of the parent isospin order, we always expect a discontinuous behavior in Hall conductance at the onset of pocket orders.

Another experimentally accessible signature of the Berry curvature is magnetization due to orbital currents in the system ground state. The magnetization can be estimated using the approach described in Refs. 45, 46, giving ~ 3 Bohr magnetons per electron for the parameters used in Fig 2 d). This is few times larger than the orbital magnetic moments of electrons in a Landau level, which are readily measurable.

In conclusion, we predict that exchange interactions drive the pocket polarization that emerges on top of an isospin polarized phase in field-biased BG. This new order further breaks the crystallographic symmetries in the isospin polarized parent phase. Depending on the isospin orientation of the parent phase, the pocket polarization can either break the rotation symmetry or the translation symmetry, resulting in either nematic order or an incommensurate Kekulé density wave order. The new orders arise through phase transitions showing interesting interplay with the cascade of isospin-polarized phases familiar from other flatband systems.

[1] R. Bistritzer and A. H. MacDonald, Moiré bands in twisted double-layer graphene, PNAS 108, 30 (2011)

[2] E. J. Mele, Commensuration and interlayer coherence in twisted bilayer graphene, Phys. Rev. B 81, 161405(R) (2010)

[3] E. Suárez Morell, J. D. Correa, P. Vargas, M. Pacheco, and Z. Barticevic, Phys. Rev. B 82, 121407 (R) (2010)

[4] J. M. B. Lopes dos Santos, N. M. R. Peres, and A. H. Castro Neto, Phys. Rev. Lett. 99, 256802 (2007)

[5] Y. Cao, V. Fatemi, S. Fang, K. Watanabe, T. Taniguchi, E. Kaxiras, and P. Jarillo-Herrero, Nature 556, 43 (2018).

[6] Y. Cao, V. Fatemi, A. Demir, S. Fang, S. L. Tomarken, J. Y. Luo, J. D. Sanchez-Yamagishi, K. Watanabe, T. Taniguchi, E. Kaxiras, R. C. Ashoori, and P. Jarillo-Herrero, Nature 556, 80 (2018).

[7] J. Kang and O. Vafek, Strong coupling phases of partially filled twisted bilayer graphene narrow bands, Phys. Rev. Lett. 122, 246401 (2019)

[8] M. Xie and A. H. MacDonald, Nature of the correlated insulator states in twisted bilayer graphene, Phys. Rev. Lett. 124, 097601 (2020)

[9] M. Ochi, M. Koshino, and K. Kuroki, Possible correlated insulating states in magic-angle twisted bilayer graphene under strongly competing interactions, Phys. Rev. B 98, 081102(R) (2018)

[10] Ferromagnetic Mott state in twisted graphene bilayers at the magic angle, K. Seo, V. N. Kotov, and B. Uchoa, Phys. Rev. Lett. 122, 246402 (2019)

[11] F. Wu and S. Das Sarma, Ferromagnetism and superconductivity in twisted double bilayer graphene, Phys. Rev. B 101, 155149 (2020)

[12] F. Wu and S. Das Sarma, Collective Excitations of Quantum Anomalous Hall Ferromagnets in Twisted Bilayer Graphene, Phys. Rev. Lett. 124, 046403 (2020)

[13] A. L. Sharpe, E. J. Fox, A. W. Barnard, J. Finney, K. Watanabe, T. Taniguchi, M. A. Kastner, D. Goldhaber-Gordon, Emergent ferromagnetism near three-quarters filling in twisted bilayer graphene, Science, 365, 6453, 605-608 (2019)

[14] M. Serlin, C. L. Tschirhart, H. Polshyn, Y. Zhang, J. Zhu, K. Watanabe, T. Taniguchi, L. Balents, A. F. Young. Intrinsic quantized anomalous Hall effect in a moiré heterostructure. Science, 367, 6480 (2020)

[15] C. L. Tschirhart, M. Serlin, H. Polshyn, A. Shragai, Z. Xia, J. Zhu, Y. Zhang, K. Watanabe, T. Taniguchi, M. E. Huber, A. F. Young, Imaging orbital ferromagnetism in a moiré Chern insulator, Science, 372, 6548, (1323-1327), (2021).

[16] J. F. Dodaro, S. A. Kivelson, Y. Schattner, X. Q. Sun, and C. Wang, Phases of a phenomenological model of twisted bilayer graphene, Phys. Rev. B 98, 075154 (2018)

[17] S. Liu, E. Khalaf, J. Y. Lee, and A. Vishwanath, "Nematic topological semimetal and insulator in magic angle bilayer graphene at charge neutrality," Phys. Rev. Research 3, 013033 (2021).

[18] A. Kerelsky, L. McGilly, D. M. Kennes, L. Xian, M. Yankowitz, S. Chen, K. Watanabe, T. Taniguchi, J. Hone, C. Dean, A. Rubio, and A. N. Pasupathy, Nature 572, 95 (2019).

[19] Y. Choi, J. Kemmer, Y. Peng, A. Thomson, H. Arora, R. Polski, Y. Zhang, H. Ren, J. Alicea, G. Refael, F. von Oppen, K. Watanabe, T. Taniguchi, and S. Nadj-Perge, Nat. Phys. 15, 1174 (2019).

[20] Y. Jiang, X. Lai, K. Watanabe, T. Taniguchi, K. Haule, J. Mao, and E. Y. Andrei, Nature 573, 91 (2019).

[21] Y. Cao, D. R. Legrain, J. M. Park, F. N. Yuan, K. Watanabe, T. Taniguchi, R. M. Fernandes, L. Fu, P. Jarillo-Herrero, arXiv:2004.04148 (2020).

[22] F. Guinea and N. R. Walet, Electrostatic effects, band distortions, and superconductivity in twisted graphene bilayers, PNAS 115 (52) 13174-13179 (2018)

[23] H. Isobe, N. F. Q. Yuan, and L. Fu, Unconventional Superconductivity and Density Waves in Twisted Bilayer Graphene, Phys. Rev. X 8, 041041 (2018)

[24] V. Kozii, H. Isobe, J. W. F. Venderbos, and L. Fu, Nematic superconductivity stabilized by density wave fluctuations: Possible application to twisted bilayer graphene, Phys. Rev. B 99, 144507 (2019)

[25] C. Xu and L. Balents, Topological Superconductivity in Twisted Multilayer Graphene, Phys. Rev. Lett. 121, 087001 (2018)

[26] Y.-P. Lin and R. M. Nandkishore, Chiral twist on the high-Tc phase diagram in moiré heterostructures, Phys. Rev. B 100, 085136 (2019)

[27] H. Zhou, Y. Saito, L. Cohen, W. Huynh, C. Patterson, F. Yang, T. Taniguchi, K. Watanabe, and A. F. Young, Isospin magnetism and spin-triplet superconductivity in Bernal bilayer graphene, arXiv: 2110.11317

[28] H. Zhou, T. Xie, A. Ghazaryan, T. Holder, J. R. Ehrets, E. M. Spanton, T. Taniguchi, K. Watanabe, E. Berg, M. Serbyn, A. F. Young. Half and quarter metals in rhombohedral trilayer graphene, arXiv:2104.00653.

[29] V. Cvetkovic, O. Vafek, Topology and symmetry breaking in ABC trilayer graphene, arXiv:1210.4923

[30] Y. Lee, S. Che, J. Velasco Jr., D. Tran, J. Baima, F. Mauri, M. Calandra, M. Bockrath, C. N. Lau, Gate Tunable Magnetism and Giant Magnetoresistance in ABC-stacked Few-Layer Graphene, arXiv:1911.04450

[31] Electronic properties of a biased graphene bilayer E. V. Castro, K. S. Novoselov, S. V. Morozov, N. M. R. Peres, J. M. B. Lopes dos Santos, J. Nilsson, F. Guinea, A. K. Geim and A. H. Castro Neto

[32] T. Stauber, E. V. Castro, N. A. P. Silva and N. M. R. Peres, J. Phys.: Condens. Matter 20 335207 (2008)

[33] H. Min, G. Borghi, M. Polini, and A. H. MacDonald,Pseudospin magnetism in graphene, Phys. Rev. B 77, 041407(R) (2008)

[34] R. E. Throckmorton and S. Das Sarma, Quantum multicriticality in bilayer graphene with a tunable energy gap Phys. Rev. B 90, 205407 (2014)

[35] J. Jung, M. Polini, and A. H. MacDonald, Persistent current states in bilayer graphene, Phys. Rev. B 91, 155423 (2015)

[36] Yang-Zhi Chou, Fengcheng Wu, Jay D. Sau, Sankar Das Sarma, Acoustic-phonon-mediated superconductivity in Bernal bilayer graphene, arXiv:2110.12303

[37] Y. Saito, F. Yang, J. Ge, et al. Isospin Pomeranchuk effect in twisted bilayer graphene. Nature 592, 220–224 (2021).

[38] U. Zondiner, A. Rozen, D. Rodan-Legrain, et al. Cascade of phase transitions and Dirac revivals in magic-angle graphene. Nature 582, 203–208 (2020).

[39] A. Rozen, J. M. Park, U. Zondiner, et al. Entropic evidence for a Pomeranchuk effect in magic-angle graphene. Nature 592, 214–219 (2021).

[40] Y. Choi, H. Kim, Y. Peng, et al. Correlation-driven topological phases in magic-angle twisted bilayer graphene. Nature 589, 536–541 (2021).

[41] A. T. Pierce, Y. Xie, J. M. Park, E. Khalaf, S. H. Lee, Y. Cao, D. E. Parker, P. R. Forrester, S. Chen, K. Watanabe, T. Taniguchi, A. Vishwanath, P. Jarillo-Herrero, A. Yacoby, Unconventional sequence of correlated Chern insulators in magic-angle twisted bilayer graphene, arXiv: 2101.04123

[42] A. S. Mayorov, D. C. Elias, M. Mucha-Kruczynski, R. V. Gorbachev, T. Tudorovskiy, A. Zhukov, S. V. Morozov, M. I. Katsnelson, V. I. Fal'ko, A. K. Geim, and K. S. Novoselov, Science 333, 860 (2011).

[43] J. Velasco Jr., L. Jing, W. Bao, Y. Lee, P. Kratz, V. Aji, M. Bockrath, C. N. Lau, C. Varma, R. Stillwell, D. Smirnov, F. Zhang, J. Jung, and A. H. MacDonald, Nat. Nanotechnol. 7, 156 (2012).

[44] E. McCann and M. Koshino, The electronic properties of bilayer graphene, Rep. Prog. Phys. 76 056503 (2013)

[45] Di Xiao, Ming-Che Chang, and Qian Niu, Berry phase effects on electronic properties, Rev. Mod. Phys. 82, 1959 (2010)

[46] F.Aryasetiawan, K.Karlsson, Modern theory of orbital magnetic moment in solids, In: Journal of Physics and Chemistry of Solids. 128, 87-108 (2019)

[47] See Supplementary Information.

SUPPLEMENTARY INFORMATION FOR "ISOSPIN FERROMAGNETISM AND MOMENTUM POLARIZATION IN BILAYER GRAPHENE"

A. Field-biased bilayer graphene bandstructure

1. *Two-band single-particle Hamiltonian*

The two-layer model is derived [44] under the assumption that intra- and interlayer hoppings (A1B1 and A2B1-type terms in the original Hamiltonian, which are 3.16 eV and 0.38 eV, correspondingly) are much larger than all the other energy scales. The single-particle Hamiltonian can be written as:

$$H_0 = \sum_{\boldsymbol{p}} \psi_i^\dagger \left[h_0 + h_t + h_a + h_{D'}\right]_{ij} \psi_j \tag{S1}$$

$$h_0 = h_1(\boldsymbol{p})\Sigma_1 + h_2(\boldsymbol{p})\Sigma_2 + D\sigma_3 \tag{S2}$$

$$h_t = v_3\left(p_2\Lambda_1 + p_1\Lambda_2\right) \tag{S3}$$

$$h_a = \frac{1}{2m_a}p^2 \tag{S4}$$

$$h_{D'} = -D\frac{p^2}{p_D^2}\sigma_3 \tag{S5}$$

Note that we rotated the basis by 90° with respect to Ref. [44]. Here h_0 is the minimal model Hamiltonian that we start our consideration from in Eq. (1). h_t produces the trigonal warping; h_a produces the particle-hole asymmetry and $h_{D'}$ is the momentum-dependent contribution that is proportional to the displacement field with $p_D \approx 0.058/a_{\mathrm{CC}}$ a D-independent constant (see Table II). The matrices are:

$$\Sigma_1 = \sigma_1,\ \Sigma_2 = \tau_3\sigma_2,\ \Lambda_1 = \tau_3\sigma_1,\ \Lambda_2 = \sigma_2 \tag{S6}$$

$$\tag{S7}$$

and the coefficients of h_0 can be written as:

$$h_1(\boldsymbol{p}) = -\frac{1}{2m}\left(p_2^2 - p_1^2\right) \tag{S8}$$

$$h_2(\boldsymbol{p}) = \frac{1}{2m}\left(2p_1p_2\right). \tag{S9}$$

We measure the energies in meV and the momentum is made dimensionless by multiplying by the carbon-carbon atom distance $a_{\mathrm{CC}} = 1.46$ Å. The relevant system parameters are given in Table II

parameter	value	parameter	value
a	2.46 Å	v	1.1×10^6 m/s
γ_0	3.16 eV	v_3	1.3×10^5 m/s
γ_1	0.381 eV	v_4	4.8×10^4 m/s
γ_3	0.38 eV	m	0.028 m_e
γ_4	0.14 eV	m_a	0.19 m_e
D	$0-100$ meV	$p_D a_{\mathrm{CC}}$	0.058

TABLE II. Parameters in the Hamiltonian computed based on values in Ref. [44]. The velocities are defined as $v_i = (\sqrt{3}/2)a\gamma_i$ ($\hbar = 1$ throughout the Supplement). The BG band mass is defined as $m = \gamma_1/2v^2 \approx 0.028m_{\mathrm{e}}$.

2. *Projection on the conduction band*

The projection to conduction band discussed in main text is formally written as following transform:

$$M \to \tilde{M} = \mathrm{tr}_\sigma(\hat{P}M), \tag{S10}$$

where tr_σ is the partial trace over sublattice degrees of freedom, the projection operator $\hat{P}$ is defined as

$$\hat{P} = \frac{1}{2}\left(\frac{h_0(\boldsymbol{p})}{E(\boldsymbol{p})} + 1\right), \quad E(p) = \sqrt{D^2 + \left(\frac{p^2}{2m}\right)^2}. \tag{S11}$$

After projection, the single-particle part of the minimal model Hamiltonian becomes diagonal

$$\tilde{H}_0 = \sum_{i\boldsymbol{p}} E(\boldsymbol{p})\tilde{\psi}^\dagger_{i,\boldsymbol{p}}\tilde{\psi}_{i,\boldsymbol{p}}, \quad i = K\uparrow, K\downarrow, K'\uparrow, K'\downarrow \tag{S12}$$

where $\tilde{\psi}_{i,p}$ is the field operator of conduction band electrons in two valleys and two spins. From now on, we write the spin indices explicitly.

In this paper, we focus on the effect of electron-electron interaction, which we modeled as a density-density coupling:

$$H_{int} = \sum_{\boldsymbol{p}\boldsymbol{p}'\boldsymbol{q}} V_{\boldsymbol{q}}\psi^\dagger_{i,\boldsymbol{p}}\psi^\dagger_{j,\boldsymbol{p}'}\psi_{j,\boldsymbol{p}'-\boldsymbol{q}}\psi_{i,\boldsymbol{p}+\boldsymbol{q}} \tag{S13}$$

At large D, the form of density-density interaction is invariant under projection:

$$\tilde{H}_{int} = \sum_{\boldsymbol{p}\boldsymbol{p}'\boldsymbol{q}} V_{\boldsymbol{q}}\tilde{\psi}^\dagger_{i,\boldsymbol{p}}\tilde{\psi}^\dagger_{j,\boldsymbol{p}'}\tilde{\psi}_{j,\boldsymbol{p}'-\boldsymbol{q}}\tilde{\psi}_{i,\boldsymbol{p}+\boldsymbol{q}} \tag{S14}$$

Here, similar to Eq.(S12), i and j take values $K\uparrow$, $K\downarrow$, $K'\uparrow$, $K'\downarrow$.

B. Estimating interaction strength V

In the main text, when numerically calculating the phase diagram, we are using the value of V to represent the strength of exchange interaction. Here, we provide an estimate for the values of V.

The interaction strength we used in our model in main text should correspond to the strength of the screened Coulomb interaction at the relevant momentum, which is Fermi momentum p_0, i.e.

$$V = \tilde{V}_{p_0}. \tag{S15}$$

Accounting for Thomas-Fermi screening, the screened Coulomb potential takes the following form

$$\tilde{V}_{p_0} = \frac{V_{p_0}}{1 + V_{p_0}\Pi_{p_0}}, \tag{S16}$$

where Π_{p_0} is the polarization function at Fermi momentum. We estimate this quantity using the value of density of states at Fermi surface ν_0. When the band is flat compared to the interaction energy, which is the case of our interest, we have

$$\nu_0 V_{p_0} \gg 1 \tag{S17}$$

In this regime, the screened Coulomb interaction is approximately

$$\tilde{V}_{p_0} = \frac{1}{\nu_0}. \tag{S18}$$

Therefore, we can estimate the interaction as

$$V \sim \frac{1}{\nu_0} \sim 10^3 \text{ meV nm}^2 \tag{S19}$$

where we have used $\nu_0 \sim n/W \sim 10^{-3}$ meV nm^{-2}, where n is the carrier density $n \sim 10^{12}$ cm^{-2}, $W \sim 10$ meV is the Fermi energy measured from the band bottom at this carrier density.

C. A symmetry-based analysis of the isospin polarized states

Importantly, we can understand the symmetry aspects of different orders regardless of detailed knowledge of which order is ultimately favored. Below, we describe the possible order types, classify them through the symmetry of our problem. For simplicity, we focus on the case of phase 1, where only one of the isospin species is populated. Other orders can be studied in a similar manner. In this phase the order parameter is simply a projection onto the state with a given valley-spin orientation. Therefore, it takes the form of

$$O_1 = |v\rangle\langle v| \tag{S20}$$

where v is an arbitrary normalized complex-valued four-component spinor in the isospin space, $|v\rangle = (\alpha_1|u_1\rangle, \alpha_2|u_2\rangle)^{\mathrm{T}}$ where $|u_1\rangle, |u_2\rangle$ are arbitrary normalized two-component state vectors in the spin subspace, α_1, α_2 are positive real numbers, $\alpha_1^2 + \alpha_2^2 = 1$. Overall phases are absorbed in $|u_1\rangle$ and $|u_2\rangle$. The symmetry analysis of the Pauli matrices in valley basis (see Table I) indicates that $\tau_{1,2}$ and τ_3 transform under different irreducible representations. Thus, an order parameter containing $\tau_{1,2}$ matrices and another one containing τ_3 corresponds to different broken symmetries. Therefore, to classify orders by symmetry, we look for an order parameter, O, that contains τ_3 or $\tau_{1,2}$ matrices only, but not a mixture of τ_3 and $\tau_{1,2}$. This gives two possible types of the order parameter with distinct symmetry: $O_1^z = \frac{1}{4}(1 \pm \tau_3)(1 + \boldsymbol{s}\cdot\boldsymbol{m})$ and $O_1^{xy} = \frac{1}{4}(1 + \gamma_1\tau_1 + \gamma_2\tau_2)(1 + \boldsymbol{s}\cdot\boldsymbol{m})$. Here, $\boldsymbol{m}$ is an arbitrary vector determining the spin direction, and (γ_1, γ_2) is an arbitrary normalized real-valued vector. The order O_1^z represents a valley imbalance order, which transforms under $A_{2,\Gamma}$ and thus, features a breakdown of the mirror symmetry that swaps the two valleys. The other option, O_1^{xy}, corresponds to the intervalley coherent order that transforms under $E_{\pm K}$. It breaks the three-fold rotation, reflection and translation symmetries of the original model. This aspect clearly differentiates the AB bilayer graphene from the case of ABC trilayer: in the latter, the intervalley coherent state does not break the C_3 rotation symmetry [29]. The symmetry classification of possible orders in AB bilayer graphene is summarized in Table I in the main text.

Our symmetry analysis allows us to identify two observables that distinguish the valley imbalance and intervalley coherent orders in phase 1. These are anisotropy of conductivity and a spatial charge density wave modulation. For valley imbalance order O_1^z, neither rotation nor translation symmetry of the space group is broken, so the conductivity is isotropic and there is no spatial pattern. In comparison, for the valley coherence order O_1^{xy}, both rotation and translation symmetries are broken. The broken rotation symmetry leads to an anisotropic conductivity, whereas the broken translation symmetry leads to a spatial pattern with momentum $2K$, i.e. a Kekulé charge density wave. On a different note, the temporal symmetry can be probed by the Hall conductance. For the valley imbalance order O_1^z where time reversal symmetry is broken, the Hall conductivity is nonvanishing. In comparison, the intervalley coherent order O_1^{xy} preserves time reversal symmetry, guaranteeing a vanishing Hall conductance. These observables are summarized in the last three columns in Table I in the main text.

D. Three-pocket model

In this section, we explain how we extract the parameters p_* and m_* we used in three-pocket model from the realistic BG band structure. As we only care about the band dispersion near the band minima, we model the three-pocket band structure using three isotropic parabolic bands:

$$H_i(\boldsymbol{p}) = \frac{(\boldsymbol{p} - \boldsymbol{k}_i)^2}{2m_*}, \quad i = 1, 2, 3 \tag{S21}$$

where i labels the pockets, $p_i's$ are the centers of pockets, corresponding to three minima of the conduction band:

$$\boldsymbol{k}_1 = k_*(0, 1), \quad \boldsymbol{k}_2 = k_*(-\frac{\sqrt{3}}{2}, -\frac{1}{2}), \quad \boldsymbol{k}_3 = k_*(\frac{\sqrt{3}}{2}, -\frac{1}{2}). \tag{S22}$$

where we specify the values of k_* and m_* below.

In order to relate the three-pocket bandstructure represented by three parabolas to the single-particle bandstructure shown before, we first adopt a minimal model that possesses thee pockets at large displacement field D. This model has the Hamiltonian

$$H_{3-p}^{min} = \sum_{\boldsymbol{p}} \psi_{i\boldsymbol{p}}^\dagger \left[h_0(\boldsymbol{p}) + h_t(\boldsymbol{p}) + h_{D'}(\boldsymbol{p})\right]_{ij} \psi_{j\boldsymbol{p}} \tag{S23}$$

We find the value of k_* by expanding in large D and treating the trigonal warping term perturbatively:

$$k_*(D) \approx p_D \left(\frac{4}{75}\frac{E_D}{D} + \frac{4}{5}\frac{D}{E_D} \right), \quad E_D = \frac{p_D^2}{2m} \approx 0.2 \text{ eV}, \tag{S24}$$

In the main text, we used the expression $k_*(D)$ given in Eq.(S24) when numerically computing phase diagram. But when estimating the validity condition of toy model, we used the value of k_* at $D = 100$meV for simplicity, which is $k_*(100\text{meV}) \approx 0.03/a_{\text{CC}}$.

The mass m_* is a parameter that we introduced in the three-pocket toy model to mimic the bottom of the conduction band from (S23). As we are interested in instabilities, the most important quantity we need to mimic with toy model is the density of states. Therefore, below, we determine the value of m_* in our toy model so that it reproduces the density of states of the original model. The Hamiltonian Eq.(S23) near one of the minimum takes the following form

$$H(\boldsymbol{k}_1 + \delta\boldsymbol{p}) = \frac{\delta p_x^2}{2m_{*\perp}} + \frac{\delta p_y^2}{2m_{*\parallel}} \tag{S25}$$

where

$$m_{*\parallel} = 0.57m\frac{E_D D}{0.07E_D^2 + D^2}, \quad m_{*\perp} = \frac{0.18 p_D}{v_3} \tag{S26}$$

The density of states in the model (S23) is given by

$$\nu = \frac{1}{2\pi}\sqrt{m_{*\perp} m_{*\parallel}}. \tag{S27}$$

Therefore, to reproduce the same density of states in our toy model Eq.(10), we set $m_* = \sqrt{m_{*\perp} m_{*\parallel}}$.

E. Exchange energy in the three-pocket model

In this section, we calculate the exchange energy discussed in main text:

$$E_{ex}^{(N)} = -\sum_{i,j=1}^{N}\sum_{\boldsymbol{p},\boldsymbol{p}'}\frac{1}{2}V_{\boldsymbol{p}-\boldsymbol{p}'+\boldsymbol{k}_{ij}} n_{\boldsymbol{p}} n_{\boldsymbol{p}'}, \quad V_{\boldsymbol{p}-\boldsymbol{p}'} = \frac{2\pi e^2}{|\boldsymbol{p}-\boldsymbol{p}'|}, \quad n_{\boldsymbol{p}} = 1 - \theta(|p| - p_0). \tag{S28}$$

where $\boldsymbol{k}_{ij} = \boldsymbol{k}_{*i} - \boldsymbol{k}_{*j}$ is the momentum difference between two pocket centers. Exchange energy takes the form of a convolution. Therefore, we evaluate it by performing Fourier transform:

$$V(r) = \frac{e^2}{|r|} = \int \frac{d^2p}{(2\pi)^2} e^{i\boldsymbol{p}\cdot\boldsymbol{r}} V_{\boldsymbol{p}} \tag{S29}$$

and

$$n(x) = \int \frac{d^2p}{(2\pi)^2} e^{i\boldsymbol{p}\cdot\boldsymbol{r}} n_{\boldsymbol{p}} \tag{S30}$$

Then, the exchange energy can be written as

$$E_{ex}^{(N)} = -\frac{1}{2}\sum_{ij}\int d^2r V(\boldsymbol{r}) n(\boldsymbol{r})^2 e^{i\boldsymbol{k}_{ij}\cdot\boldsymbol{r}} = -\frac{1}{2}\sum_{ij}\int_0^\infty V(r) n(r)^2 2\pi J_0(r|k_{ij}|) x dx \tag{S31}$$

To evaluate this quantity, we need to first work out the form of $n(r)$:

$$n(r) = \int_{|p|<p_0} \frac{dp_x dp_y}{4\pi^2} e^{ip_x r} = \int \frac{dp_x}{2\pi^2}\sqrt{p_0^2 - p_x^2} e^{ip_x r} = \frac{p_0^2}{2\pi^2}\int_{-\frac{\pi}{2}}^{\frac{\pi}{2}} d\theta \cos^2\theta e^{iz\sin\theta} \tag{S32}$$

$$= \frac{p_0^2}{8\pi}\left[J_2(z) + 2J_0(z) + J_{-2}(z)\right] = \frac{p_0^2}{4\pi}\left[J_2(z) + J_0(z)\right] \tag{S33}$$

where $z = rp_0$. We finally arrive at

$$E_{ex}^{(N)} = -\frac{e^2 p_0^3}{16\pi}\sum_{ij}\int_0 dz \left[J_2(z) + J_0(z)\right]^2 J_0\left(\frac{z|k_{ij}|}{p_0}\right) \tag{S34}$$

F. The Berry curvature and orbital magnetization

It is straight forward to compute the Berry curvature using the Hamiltonian Eq. (S23). Below, we first explain how we compute the Berry curvature in realistic BG model and obtain the result of Fig.2. We take the form of the Hamiltonian projected to conduction band in Eq. (S23), and rewrite it as

$$H_{3-p}^{min} = \sum_{\boldsymbol{p}} \psi_{i\boldsymbol{p}}^{\dagger} \boldsymbol{h}(\boldsymbol{p}) \cdot \boldsymbol{\tau}_{ij} \psi_{j\boldsymbol{p}}, \quad \boldsymbol{h}(p) \cdot \boldsymbol{\tau} = [h_0(\boldsymbol{p}) + h_t(\boldsymbol{p}) + h_{D'}(\boldsymbol{p})] \tag{S35}$$

where $\boldsymbol{\tau} = (\tau_1, \tau_2, \tau_3)$. Then the Berry curvature is given by

$$\Omega_{\boldsymbol{p}} = \frac{1}{2} \frac{\boldsymbol{h}}{|\boldsymbol{h}|} \cdot \left(\frac{\partial \boldsymbol{h}(\boldsymbol{p})}{\partial p_1} \times \frac{\partial \boldsymbol{h}(\boldsymbol{p})}{\partial p_2} \right). \tag{S36}$$

In main text Fig.2 we use Eq.(S36) to numerically compute the Berry curvature.

Next, we estimate the orbital magnetization which arises from Berry curvature. Below, we recap the derivation of orbital moment described in Ref. 45 and 46, and apply it to our model.

As a starting point, we consider the current flowing along the sample boundary, treating it as an anomalous current arising due to Berry's curvature and driven by the filed due to spatially varying trapping potential V. This gives a current value

$$I = e \int dx n(x) v(x) = e \int dx \int \frac{d^2p}{(2\pi)^2} \Omega_{\boldsymbol{p}} f(\epsilon_{\boldsymbol{p}} - \mu + V) \frac{\partial V}{\partial x} \tag{S37}$$

where x is the coordinate in the direction perpendicular to the boundary. The magnetization per unit area is therefore given by

$$M = \frac{IA}{A} = e \int_0^{\mu} \Omega_{FS}(\mu - V) dV, \quad \Omega_{FS}(E) = \int \frac{d^2p}{(2\pi)^2} \Omega_{\boldsymbol{p}} f(\epsilon_{\boldsymbol{p}} - E) \tag{S38}$$

To estimate the magnetization value, we apply Eq. (S38) to the three-pocket model used in the main text, taking Ω_p as a constant $\Omega_p \sim \Omega$ within the Fermi sea. This gives

$$\frac{M}{\mu_B} \sim \frac{N m_* e \Omega \tilde{\mu}^2}{4\pi} = \frac{N m_* m_{\mathrm{e}} \Omega \tilde{\mu}^2}{2\pi}. \tag{S39}$$

where μ_B is the Bohr magneton, m_{e} is the electron mass, N is the number of pockets that are filled, $\tilde{\mu}$ is Fermi level measured from the bottom of the band. We estimate M for the case shown in Fig.2, where $N = 3$, $\tilde{\mu} = 10$ meV, $m_* = 2\pi\nu_* = 3 \times 10^{-4}$ meV^{-1} nm^{-2} and $\Omega \sim 15$ nm^2 [extracted from Fig. 2], we find

$$\frac{M}{\mu_B} \sim 3 \times 10^{-3} \mathrm{nm}^{-2} \sim 3n \tag{S40}$$

where we used electron density $n = 10^{11}$ cm^{-2}, a value corresponding to the regime where pocket polarization is expected. This predicts a sizable orbital magnetic moment of ~ 3 Bohr magnetons per conduction electron.